


## Article

# Effect of Magnesium Salt ( $\text{MgCl}_2$ and $\text{MgSO}_4$ ) on the Microstructures and Properties of Ground Granulated Blast Furnace Slag (GGBFS)-Based Geopolymer

Kun Zhang <sup>1</sup>, Kaiqiang Wang <sup>1</sup>, Zhimao Liu <sup>1</sup>, Zhiwu Ye <sup>1</sup>, Baifa Zhang <sup>2,\*</sup> , Deng Lu <sup>1,\*</sup>, Yi Liu <sup>2</sup>, Lijuan Li <sup>2</sup> and Zhe Xiong <sup>2</sup>

<sup>1</sup> China Construction Third Engineering Bureau Group Co., Ltd., Wuhan 430074, China; zhangk@cscec.com (K.Z.); wangkaiqiang@cscec.com (K.W.); lzm\_24@163.com (Z.L.); yzw1512@cscec.com (Z.Y.)

<sup>2</sup> School of Civil and Transportation Engineering, Guangdong University of Technology, Guangzhou 510006, China; 15374213357@163.com (Y.L.); lij@gdut.edu.cn (L.L.); gdgyxz263@gdut.edu.cn (Z.X.)

\* Correspondence: zhangbaifa@gdut.edu.cn (B.Z.); ludeng07@126.com (D.L.)

**Abstract:** The use of seawater to prepare geopolymers has attracted significant research attention; however, the ions in seawater considerably influence the properties of the resulting geopolymers. This study investigated the effects of magnesium salts and alkaline solutions on the microstructure and properties of ground-granulated-blast-furnace-slag-based geopolymers. The magnesium salt-free  $\text{Na}_2\text{SiO}_4$ -activated geopolymer exhibited a much higher 28 d compressive strength (63.5 MPa) than the salt-free NaOH-activated geopolymer (31.4 MPa), with the former mainly containing an amorphous phase (C-(A)-S-H gel) and the latter containing numerous crystals.  $\text{MgCl}_2 \cdot 6\text{H}_2\text{O}$  addition prolonged the setting times and induced halite and Cl-hydroxalite formation. Moreover, mercury intrusion porosimetry and scanning electron microscopy revealed that the  $\text{Na}_2\text{SiO}_4$ -activated geopolymer containing 8.5 wt%  $\text{MgCl}_2 \cdot 6\text{H}_2\text{O}$  exhibited a higher critical pore size (1624 nm) and consequently, a lower 28 d compressive strength (30.1 MPa) and a more loosely bound geopolymer matrix than the salt-free geopolymer. In contrast,  $\text{MgSO}_4$  addition had less pronounced effects on the setting time, mineral phase, and morphology. The  $\text{Na}_2\text{SiO}_4$ -activated geopolymer with 9.0 wt%  $\text{MgSO}_4$  exhibited a compressive strength of 42.8 MPa, also lower than that of the salt-free geopolymer. The results indicate that  $\text{Cl}^-$  is more harmful to the GGBFS-based geopolymer properties and microstructure than  $\text{SO}_4^{2-}$  is.

**Keywords:** alkaline solution; geopolymer; ground granulated blast furnace slag; magnesium salt; microstructure



**Citation:** Zhang, K.; Wang, K.; Liu, Z.; Ye, Z.; Zhang, B.; Lu, D.; Liu, Y.; Li, L.; Xiong, Z. Effect of Magnesium Salt ( $\text{MgCl}_2$  and  $\text{MgSO}_4$ ) on the Microstructures and Properties of Ground Granulated Blast Furnace Slag (GGBFS)-Based Geopolymer. *Materials* **2022**, *15*, 4911. <https://doi.org/10.3390/ma15144911>

Academic Editors: Lik-ho Tam, Chao Wu, Ao Zhou, Zechuan Yu and F. Pacheco Torgal

Received: 16 June 2022

Accepted: 13 July 2022

Published: 14 July 2022

**Publisher's Note:** MDPI stays neutral with regard to jurisdictional claims in published maps and institutional affiliations.



**Copyright:** © 2022 by the authors. Licensee MDPI, Basel, Switzerland. This article is an open access article distributed under the terms and conditions of the Creative Commons Attribution (CC BY) license (<https://creativecommons.org/licenses/by/4.0/>).

## 1. Introduction

Alkali-activated geopolymers are inorganic cementitious materials composed of crosslinked  $[\text{AlO}_4]$  and  $[\text{SiO}_4]$  tetrahedrons, within charge-balancing hydrated alkali metal cations [1,2]. Upon the activation of a geopolymer precursor with a concentrated alkaline solution, it undergoes dissolution, rearrangement, condensation, and re-solidification [3]. Finally, a geopolymer with a three-dimensional network structure is formed after curing at ambient or slightly elevated temperatures [4]. Geopolymers exhibit excellent characteristics, such as favorable mechanical properties [5], durability [6], heavy metal solidification [7,8], and absorption [9]. In addition, their manufacturing process consumes less energy and emits less  $\text{CO}_2$  than the ordinary Portland cement (OPC) manufacturing process; thus, geopolymers have attracted considerable research attention and have been regarded as a potential alternative to OPC for preparing concrete materials [10–12]. Raw materials with sufficient amounts of reactive alumina and silica (such as clay minerals [13,14], solid waste [15–17], and other

minerals [18,19]) and solid wastes such as mine tailings [17,20], fly ash (FA) [21,22], and slag [23,24] can be directly used as geopolymer precursors. In particular, finding use for solid waste in the concrete industry promotes environmental protection.

Ground granulated blast furnace slag (GGBFS) is a solid waste produced at a large scale by the iron industry. To efficiently recycle GGBFS, its applications as an additive, as a microcrystalline glass component, and as an alternative to cement have been explored in the fields of construction and medicine [25]. Owing to its high content of glassy phase and  $\text{SiO}_2$ ,  $\text{CaO}$ , and  $\text{Al}_2\text{O}_3$ , GGBFS is a promising geopolymer precursor [26]. Thus far, GGBFS has been widely used as a raw material for geopolymer preparation and application in high-performance concrete [27], infrastructure construction [28], and composite manufacturing [29]. In India, Tembhurkar et al. [28] produced a modular toilet unit using GGBFS/FA-based geopolymer. They found that compared with traditional construction materials, GGBFS/FA-based geopolymer conserved natural resources, reduced  $\text{CO}_2$  emissions, and reduced production costs.

Concrete production consumes not only cementitious materials but also a large amount of natural resources such as fresh water, which can contribute to water shortages. Annually, approximately 1.5 billion tons of fresh water is consumed for concrete production; by 2025, two-thirds of the world population is estimated to face a water crisis [30], exacerbated by the uneven distribution of water resources [31]. With the increased demand for environmental conservation, finding an alternative to fresh water for use in construction is vital.

Construction projects on islands and offshore sites have largely increased. Therefore, the use of seawater instead of fresh water to prepare concrete has attracted increasing attention [32–34]. Wang et al. [35] found that seawater could enhance OPC hydration, resulting in microstructure densification, high crystal content, and reduced autogenous shrinkage. Several researchers have recently utilized seawater for geopolymer preparation. Rashad et al. [36] compared the effects of magnetic water, seawater, and tap water on the workability and mechanical properties of slag-based geopolymer and found that seawater, owing to its high pH and high amounts of  $\text{Cl}^-$ ,  $\text{Na}^+$ , and  $\text{SO}_4^{2-}$ , improved the flowability and compressive strength of the pastes. Jun et al. [37] comparatively studied the properties of geopolymers prepared with seawater and deionized water and concluded that seawater improved electrical resistivity and early compressive strength, attributable to the formation of Cl-bearing phases (e.g., Cl-hydrocalumite,  $\text{AlOCl}$ , and aluminum chloride hydrate). Moreover, the seawater-mixed, slag-based geopolymer exhibited a higher Cl-binding capacity than the FA-based geopolymer, owing to the differences in the Cl-bearing composition [38].

The findings of the above-mentioned studies indicate that seawater is a potential material for use in preparing alkali-activated geopolymer; however, the ions (e.g.,  $\text{Cl}^-$ ,  $\text{Mg}^{2+}$ , and  $\text{SO}_4^{2-}$ ) in seawater affect the geopolymer microstructure and chemical composition, thereby altering the geopolymer mechanical properties and durability. Several studies [39–41] have clarified the role of seawater in geopolymer preparation and confirmed that the microstructures of the as-obtained materials highly influenced their macro-properties. While numerous studies have focused on the comparative evaluation of the mechanical properties of seawater-mixed and deionized water-mixed geopolymers and on the role of  $\text{Cl}^-$  in geopolymers [37,38,42–44], few studies have examined the effects of other ions on geopolymer microstructures and properties. In particular,  $\text{SO}_4^{2-}$  may have a remarkable impact on the microstructures and properties of slag-based geopolymers [45]. Studies have reported that in geopolymers immersed in sulfate solution or seawater,  $\text{SO}_4^{2-}$  reacts with  $\text{Ca}^{2+}$  to form expandable gypsum and ettringite [46], destroying the geopolymer microstructure. These studies have also reported that Ca considerably influences the composition and properties of salt-containing, water-mixed geopolymer. Thus far, a few studies have shown that Cl-containing salts (e.g.,  $\text{KCl}$ ,  $\text{MgCl}_2$ , and  $\text{CaCl}_2$ ) induce the precipitation and crystallization of geopolymeric gels, whereas  $\text{CO}_3^{2-}$ -containing salt (e.g.,  $\text{K}_2\text{CO}_3$ ,  $\text{MgCO}_3$ , and  $\text{CaCO}_3$ ) prevents hydrolytic attacks on geopolymeric gels [47]. In other studies,  $\text{SO}_4^{2-}$  facilitates zeolite crystallization in geopolymers [48], and high

$\text{SO}_4^{2-}$  content is much more beneficial to geopolymer properties than low  $\text{SO}_4^{2-}$  content [49]. Thus, the anions considerably influence the geopolymer properties. However, the geopolymers prepared in the above-mentioned studies were based on FA or kaolinite, both of which have relatively low Ca concentrations.

In this work, considering that seawater mainly contains  $\text{Na}^+$ ,  $\text{Mg}^{2+}$ ,  $\text{Cl}^-$ , and  $\text{SO}_4^{2-}$  ions while alkaline solutions contain large amounts of  $\text{Na}^+$ , the effects of the salt ( $\text{MgCl}_2$ ,  $\text{MgSO}_4$ ) content on the mechanical properties and microstructures of alkali-activated ( $\text{NaOH}$  or  $\text{Na}_2\text{SiO}_3$  solution) GGBFS-based geopolymers were investigated, with the objective of elucidating the geopolymerization of Ca-containing precursors in salt-containing seawater. The chemical structures of different polymers were characterized via X-ray diffraction (XRD), Fourier-transform infrared (FTIR) spectroscopy, and thermogravimetric (TG) analysis. The microstructural features and composition of the geopolymers were examined via scanning electron microscopy (SEM) coupled with energy-dispersive X-ray (EDX) spectroscopy and mercury intrusion porosimetry (MIP).

## 2. Materials and Methods

### 2.1. Materials

GGBFS was purchased from Yuanheng Environmental Protection Engineering Co., Ltd., in Henan province, Nanyang, China. Its chemical composition (determined via X-ray fluorescence) by mass of oxides was as follows:  $\text{SiO}_2$  (33.21 wt%),  $\text{CaO}$  (37.14 wt%),  $\text{Al}_2\text{O}_3$  (15.76 wt%),  $\text{Fe}_2\text{O}_3$  (0.71 wt%),  $\text{MgO}$  (8.51 wt%),  $\text{TiO}_2$  (1.91 wt%), and others (2.76 wt%).  $\text{CaO}$  and  $\text{SiO}_2$  accounted for 70.35 wt% of the total GGBFS composition. The XRD patterns (Figure 1a) featured one broad peak spanning from  $19^\circ(2\theta)$  to  $40^\circ(2\theta)$ , indicating that GGBFS was mainly in the amorphous phase, with small amounts of crystals, such as calcite, akermanite, and dolomite. SEM images (Figure 1b) showed that the particles in the GGBFS were nonuniform in size and angular.

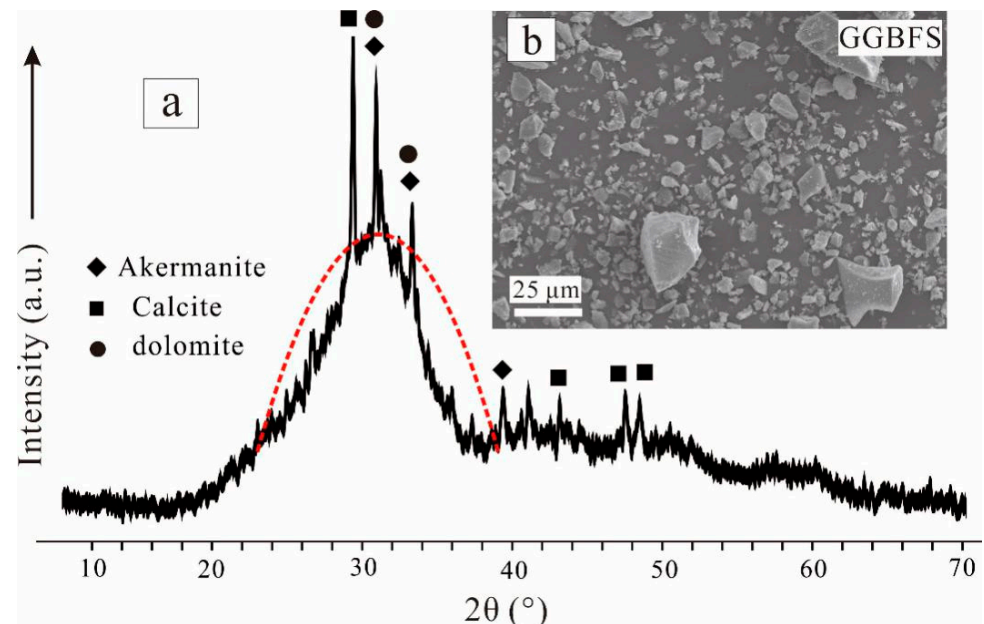


**Figure 1.** (a) XRD patterns and (b) SEM image of the GGBFS.

Chemical-grade  $\text{NaOH}$  pellets (Zhiyuan Chemical Reagent Co., Ltd., Tianjin, China; purity  $\geq 96\%$ ) and  $\text{Na}_2\text{SiO}_4$  pellets (Henyuan New Material Co., Ltd., Zhengzhou, China;  $\text{Na}_2\text{O}$  26.0 wt% and  $\text{SiO}_2$  60.0 wt%, modulus of 2.9) were used as alkali activators.  $\text{MgCl}_2 \cdot 6\text{H}_2\text{O}$  (Yongda Chemical Reagent Co., Ltd., Tianjin, China; purity  $\geq 98\%$ ) and  $\text{MgSO}_4$  (Baishi Chemical Co., Ltd., Tianjin, China; purity  $\geq 99\%$ ) were used as additives. All of the chemical agents were obtained from commercial suppliers.

## 2.2. Geopolymer Preparation

First, NaOH or Na<sub>2</sub>SiO<sub>4</sub> was added into distilled water to prepare an alkaline solution. The NaOH concentration was set to 10 mol/L, while the Na<sub>2</sub>SiO<sub>4</sub> concentration was set to 35%, with a modulus of 1.5. The desired concentrations were achieved through the controlled addition of NaOH, Na<sub>2</sub>SiO<sub>4</sub> pellets, and deionized water. As shown in Figure 2, GGBFS was mixed with an alkaline solution at a solid/liquid ratio of 0.55 to form a homogeneous paste, which was then cast into silica molds (20 × 20 × 20 mm<sup>3</sup>). To prevent water evaporation, the molds were covered with a thin polyethylene film, and the molded specimens were cured at ambient temperature for 24 h before demolding. The demolded specimens were cured at ambient temperature until the test date.

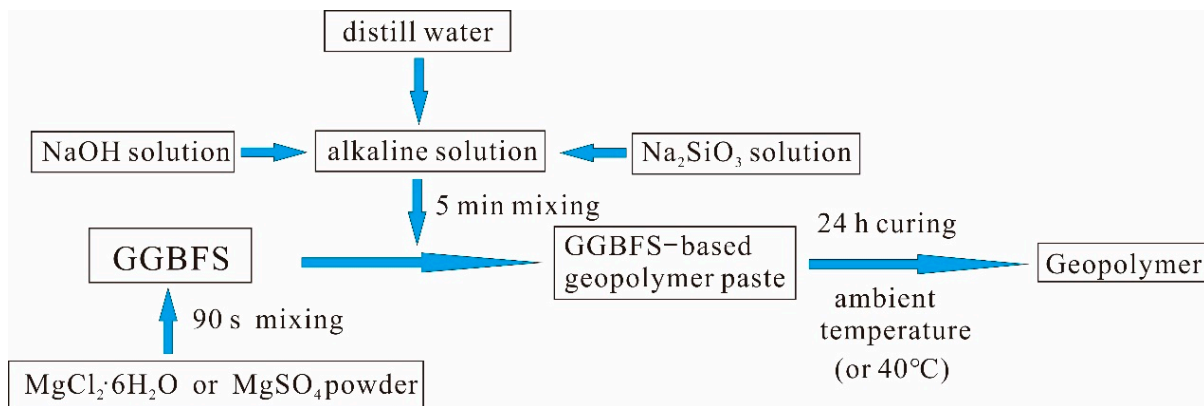


**Figure 2.** Preparation of GGBFS-based geopolymer.

The concentration of MgSO<sub>4</sub> salt in GGBFS was set to 1.0, 3.0, 5.0, 7.0, and 9.0 wt%, while, based on the number of Mg<sup>2+</sup> moles in MgSO<sub>4</sub>, the MgCl<sub>2</sub>·6H<sub>2</sub>O concentration in GGBFS was set to 1.7, 5.1, 8.5, 11.8, and 15.2 wt%. The salts were first ground into powder and then mixed with GGBFS; afterward, NaOH or Na<sub>2</sub>SiO<sub>4</sub> solution was added, and the mixture was stirred to form a homogeneous paste. The preparation process and conditions were the same as those for the activated GGBFS sample, except for the specimens containing 11.8 and 15.2 wt% MgCl<sub>2</sub>·6H<sub>2</sub>O. These two specimens could not set at ambient temperature and thus were cured at 40 °C in an oven. Herein, the specimens are denoted as G<sub>X</sub>-Cl<sub>Y</sub> or G<sub>X</sub>-S<sub>Y</sub>, where X represents the modulus of the alkaline solution and Y the salt concentration by weight, and Cl and S represent MgCl<sub>2</sub>·6H<sub>2</sub>O and MgSO<sub>4</sub>, respectively. For example, G<sub>0</sub>-Cl<sub>1.7</sub> denotes a GGBFS-based geopolymer prepared via activation with a 10 mol/L NaOH solution and containing 1.7 wt% MgCl<sub>2</sub>·6H<sub>2</sub>O.

## 2.3. Characterization Methods

According to the ASTM C191 standard test method, the initial and final setting times of the alkali-activated, GGBFS-based geopolymeric pastes were determined using Vicat apparatus (Luda Experimental Instruments Co., Ltd., Shanghai, China).

According to the GBT50081-2019 standard test method, the compressive strengths of all geopolymers cured for 1, 7, and 28 days were tested on a microcomputer-controlled electronic universal testing machine (STS100K, Yishite Instrument Co., Ltd., Xiamen, China) under a loading rate of 100 N/s. The compressive test for each group was run four times, and the average value was recorded as the compressive strength.

The XRD patterns, in the 3°(2θ)–60°(2θ) range, of the selected geopolymers cured for 28 days were obtained using a diffractometer (Bruker D8 Advance, Mannheim, Germany) with CuKα radiation operated at 40 kV, 40 mA, and a scanning speed of 3°(2θ)/min.

The FTIR spectra (64 scans, 4 cm<sup>-1</sup>) of selected geopolymers cured for 28 days were obtained using a spectrometer (Nicolet IS50, Thermo Fisher, Waltham, MA, USA) at a wavelength of 400–1800 cm<sup>-1</sup>. First, 0.8 mg of each sample was mixed with 80 mg of KBr,

and then, the mixture was ground into fine powder. The mixture was then pressed into a disk for testing.

The TG and differential scanning calorimetry (DSC) curves of selected geopolymers cured for 28 days were obtained using a thermal gravimetric analyzer (TGA 4000, PE, Holland). The powdered samples were heated between 30 °C and 900 °C at 10 °C/min.

The SEM micrographs and EDX spectra of selected geopolymers cured for 28 days were obtained using a scanning electron microscope (S-3400N-II, Hitachi, Tokyo, Japan) at an accelerating voltage of 15 kV. The samples were anchored on a conducting tape and then coated with a gold layer.

The pore size distribution of selected geopolymers was determined using a mercury porosimeter (AutoPore Iv 9510, Micromeritics, Norcross, GA, USA). The intrusion pressures ranged from 0.5 to 33,000 psi, and the equilibrium time for each applied pressure was set to 10 s.

### 3. Results and Discussion

#### 3.1. Setting Time and Compressive Strength

##### 3.1.1. Setting Time

Figure 3 shows the initial and final setting times of the geopolymers. The initial and final setting times of NaOH-activated GGBFS were slightly longer than those of Na<sub>2</sub>SiO<sub>3</sub>-activated GGBFS, demonstrating that the presence of soluble silicate favored the setting and hardening of geopolymeric pastes.

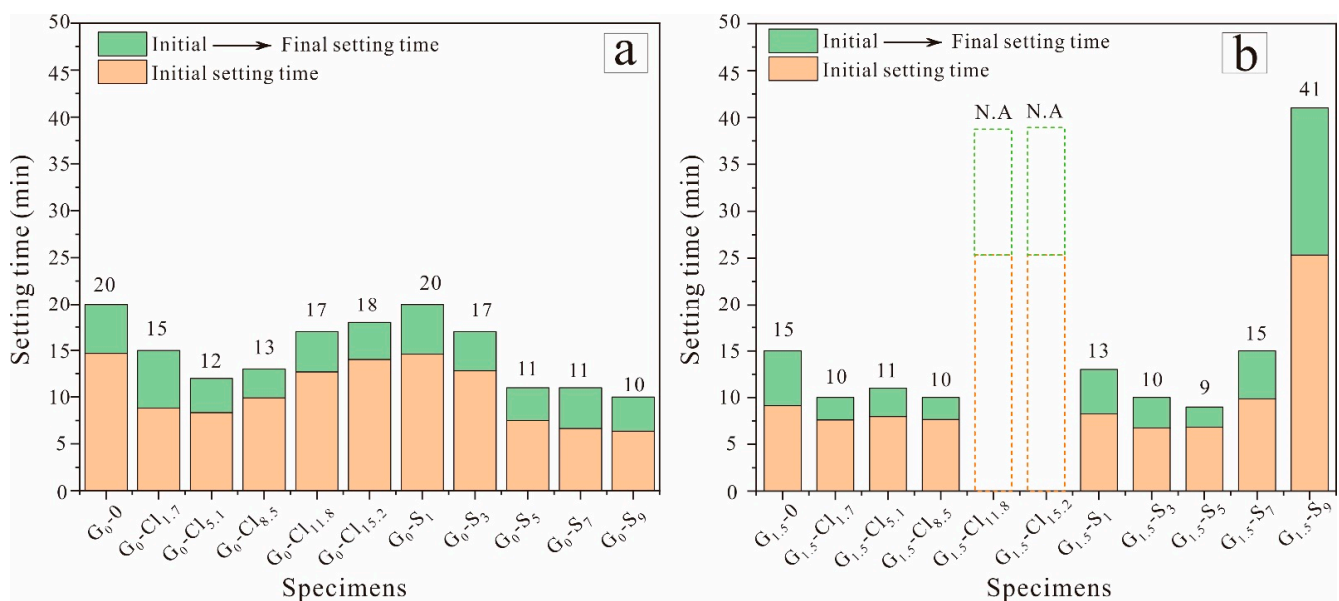


**Figure 3.** Setting times of (a) NaOH-activated and (b) Na<sub>2</sub>SiO<sub>3</sub>-activated geopolymers. (Dotted lines indicate specimens that could not set at ambient temperature).

The setting times of NaOH-activated GGBFS when increasing MgCl<sub>2</sub>·6H<sub>2</sub>O from 0 to 15.2 wt% decreased slightly from 20 to 12 min and then increased to 18 min. Meanwhile, the setting time of geopolymer (G<sub>0</sub>-0) decreased gradually from approximately 20 min to 10 min when the addition dosage of MgSO<sub>4</sub> increased from 0 to 9 wt%. Thus, the addition of a small amount of magnesium salt shortened the setting time of NaOH-activated GGBFS, possibly owing to the exothermic reaction between Mg<sup>2+</sup> and OH<sup>-</sup>. However, large amounts of OH<sup>-</sup> were consumed at a high dosage of magnesium salt, which was accompanied by alkalinity reduction and the extension of the geopolymer setting time.

Figure 3b shows that the final setting time of the Na<sub>2</sub>SiO<sub>3</sub>-activated GGBFS with 5.0 wt% MgSO<sub>4</sub> (9 min) was shorter than that of the salt-free, Na<sub>2</sub>SiO<sub>3</sub>-activated GGBFS (G<sub>1.5</sub>-0, 20 min), but the geopolymer with 9 wt% MgSO<sub>4</sub> exhibited a significantly longer

setting time (41 min). In particular, at a  $\text{MgCl}_2 \cdot 6\text{H}_2\text{O}$  dosage of  $>8.5$  wt%, the geopolymer paste could not set at the ambient temperature. At high magnesium salt concentrations, the occurrence of  $\text{Cl}^-$  and  $\text{SO}_4^{2-}$  prolonged the setting time of  $\text{Na}_2\text{SiO}_3$ -activated GGBFS relative to that of  $\text{NaOH}$ -activated GGBFS (Figure 3a).

In addition, the  $\text{Mg}^{2+}$  anion considerably influenced the setting behavior of the GGBFS-based geopolymer. At high concentrations,  $\text{Cl}^-$  tended to prolong the geopolymer setting time more than  $\text{SO}_4$ . This result is consistent with those of previous studies, which have reported that a high  $\text{Cl}^-$  concentration severely hinders the setting of GGBFS-based geopolymers [50]; however,  $\text{SO}_4^{2-}$  exhibited a less pronounced influence on the setting time of  $\text{Na}_2\text{SiO}_3$ -activated, high-calcium, FA-based geopolymers [51].

### 3.1.2. Compressive Strength

Figure 4 shows the compressive strengths of all the tested geopolymers. The compressive strengths increased with aging time. In addition, the  $\text{NaOH}$ -activated GGBFS showed much lower compressive strengths than the  $\text{Na}_2\text{SiO}_3$ -activated GGBFS. The 28 d compressive strength of  $G_{1.5-0}$  was 63.5 MPa, while that of  $G_{0-0}$  was only 31.4 MPa. Studies have also reported that the mechanical properties of geopolymers considerably improve with an increasing Si/Al ratio [52,53].

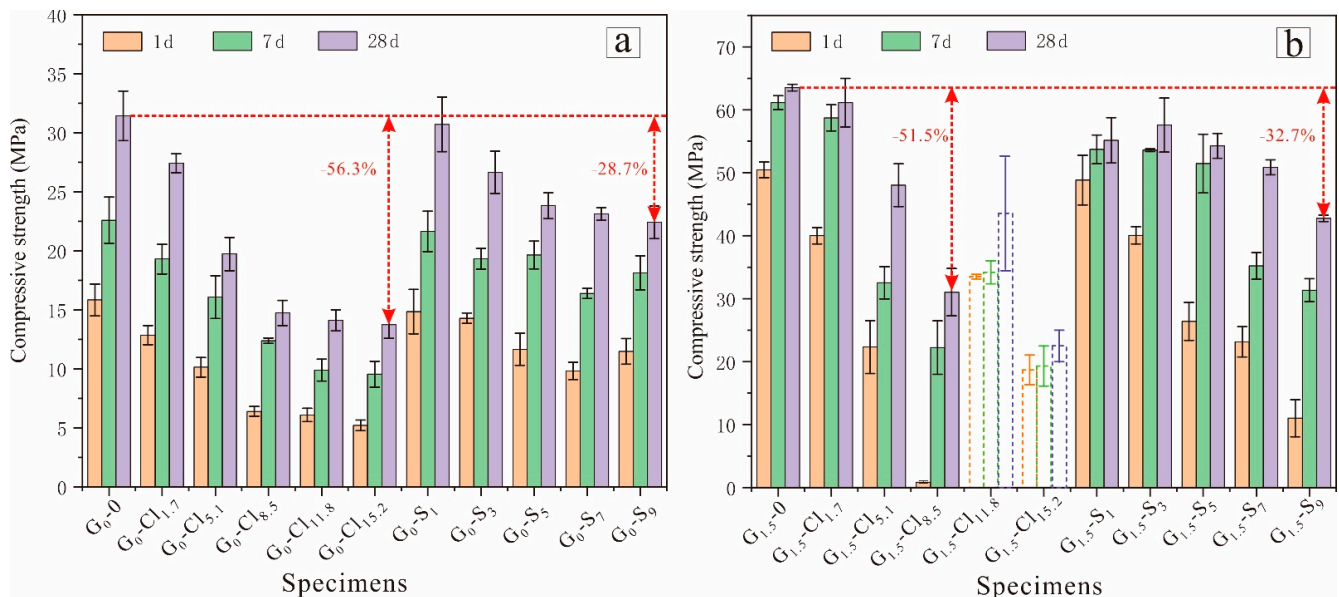


**Figure 4.** Compressive strengths of (a)  $\text{NaOH}$ -activated and (b)  $\text{Na}_2\text{SiO}_3$ -activated geopolymers (dotted lines indicate specimens cured at  $40^\circ\text{C}$ ).

Figure 4a shows that magnesium salt addition negatively affected the compressive strengths of  $\text{NaOH}$ -activated GGBFS. With an increase in the  $\text{MgCl}_2 \cdot 6\text{H}_2\text{O}$  concentration from 0 to 8.5 wt%, the 28 d compressive strength of the geopolymer decreased from 31.4 to 14.7 MPa; however, with a further increase to 15.2 wt%, the compressive strength barely changed. The  $G_0\text{-S}$  samples exhibited similar results: the 28 d compressive strengths of the geopolymer decreased from 31.4 to 23.8 MPa with an increase in the magnesium salt concentration from 0 to 5 wt% and then remained almost unchanged with a further increase. These results suggest that at a high magnesium salt concentration, the anions offset the negative effect of  $\text{Mg}^{2+}$ , thereby improving the compressive strength of the  $\text{NaOH}$ -activated, GGBFS-based geopolymer.

The addition of magnesium salts also reduced the compressive strength of  $\text{Na}_2\text{SiO}_3$ -activated GGBFS (Figure 4b), with  $\text{Cl}^-$  exhibiting a greater negative effect than  $\text{SO}_4^{2-}$ . With an increase in the  $\text{MgCl}_2 \cdot 6\text{H}_2\text{O}$  concentration from 0 to 8.5 wt%, the 1 d and 28 d compressive strengths of the geopolymer decreased significantly from 50.5 to 0.85 MPa and

from 63.5 to 30.1 MPa, respectively. Geopolymers with higher  $\text{MgCl}_2 \cdot 6\text{H}_2\text{O}$  concentrations could not set at the ambient temperature. Moreover, increasing the curing temperature improved geopolymerization; accordingly,  $G_0\text{-Cl}_{11.8}$  and  $G_0\text{-Cl}_{15.2}$  exhibited 28 d compressive strengths of 41.9 and 22.1 MPa, respectively. The geopolymer with a  $\text{MgSO}_4$  concentration of 9.0 wt% exhibited a 28 d compressive strength of 42.8 MPa, less than that of the geopolymer with 8.5 wt%  $\text{MgCl}_2 \cdot 6\text{H}_2\text{O}$  (63.5 MPa).

### 3.2. Structure of GGBFS-Based Geopolymer

#### 3.2.1. XRD Patterns

Figure 5 shows the XRD patterns of selected GGBFS-based geopolymers.  $G_0\text{-0}$  showed a different diffraction pattern from  $G_{1.5}\text{-0}$ . The XRD pattern of  $G_0\text{-0}$  featured a broad peak ranging from  $24^\circ(2\theta)$  to  $42^\circ(2\theta)$ . The peak was centered at  $32^\circ(2\theta)$  in the XRD patterns of the geopolymer but at  $30^\circ(2\theta)$  in those of GGBFS (Figure 1), indicating the formation of an amorphous geopolymer (C-(A)-S-H), which may contribute to strength development. In addition to the amorphous phase, many neoformed crystals occurred in the geopolymers. Peaks corresponding to crystal C-(A)-S-H and hydrotalcite-like ( $\text{Mg}_6\text{Al}_2(\text{CO}_3)(\text{OH})_{16} \cdot 4\text{H}_2\text{O}$ ), a Mg-layered double hydroxide phase, were identified at approximately  $29^\circ(2\theta)$  (with a  $d_{022}$  of 3.1 Å) and  $11^\circ(2\theta)$  (with a  $d_{006}$  of 7.6 Å), respectively [54,55]. Chlormagaluminite ( $(\text{Mg}, \text{Fe})_4\text{Al}_2(\text{Cl}, \text{CO}_3)(\text{OH})_{12} \cdot 2\text{H}_2\text{O}$ ), with a comparable composition and structure with hydrotalcite-like phases, was also formed. Moreover, numerous unreacted species, such as calcite and akermanite, also occurred, as they did not react with NaOH. The magnesium-salt-containing geopolymers exhibited no considerable diffraction difference; they only differed in the intensity of XRD peaks corresponding to hydrotalcite-like phases, which was attributable to the replacement of  $\text{CO}_3^{2-}$  by  $\text{Cl}^-$  or  $\text{SO}_4^{2-}$ , because the  $\text{CO}_3^{2-}$  in the interlayers of the hydrotalcite-like phases was displaceable [38].

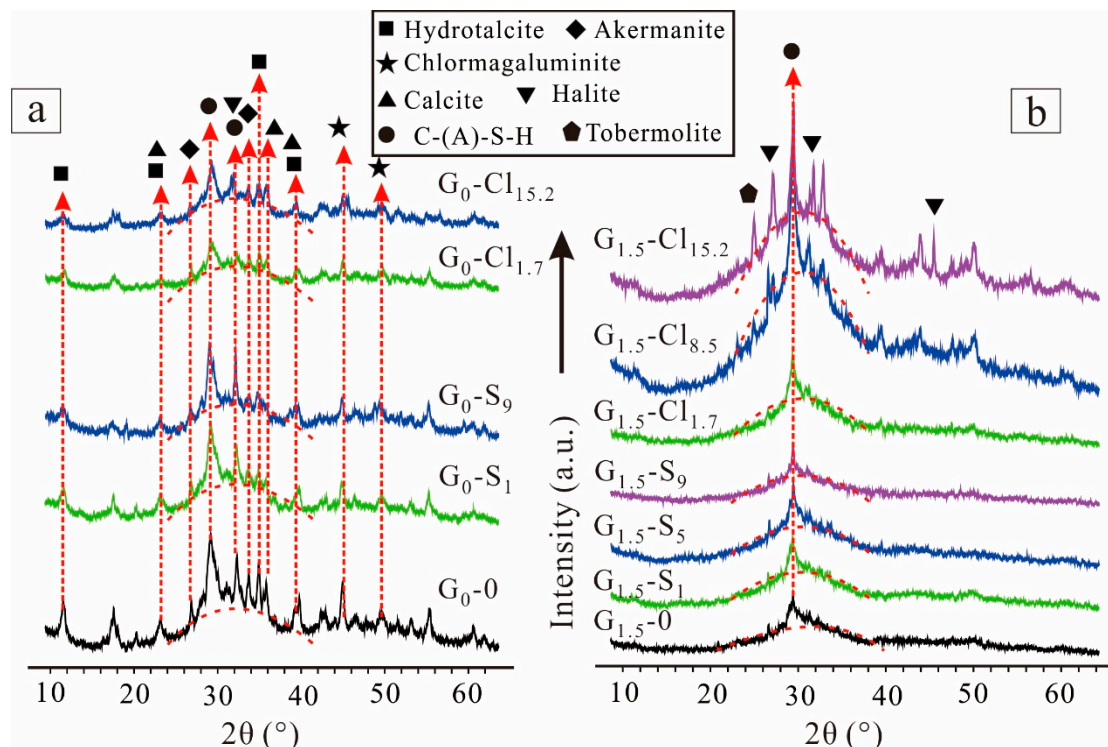


Figure 5. XRD patterns of (a) NaOH-activated and (b)  $\text{Na}_2\text{SiO}_3$ -activated geopolymers.

The XRD patterns of  $G_{1.5}\text{-0}$  showed a broad peak centered at approximately  $29^\circ(2\theta)$  (Figure 4b). Although this center shifted to a lower region after geopolymerization, the geopolymer could be concluded to have formed [56]. In addition,  $G_{1.5}\text{-0}$  contained crystal C-(A)-S-H but no other mineral, unlike  $G_0\text{-0}$ . Therefore, the soluble silica significantly affected

the geopolymerization process and the chemical composition of alkali-activated GGBFS. The XRD pattern of the geopolymer with 9 wt%  $\text{MgSO}_4$  ( $G_{1.5-S_9}$ ) was not considerably different from that of  $G_{1.5-0}$ , indicating that  $\text{Ca}^{2+}$  preferentially reacted with silicate to form C-(A)-S-H gels than with  $\text{SO}_4^{2-}$  to form gypsum ( $\text{CaSO}_4$ ). However, the determination of the occurrence form of  $\text{SO}_4^{2-}$  via an XRD test is difficult because no  $\text{SO}_4^{2-}$ -containing mineral was detected. The XRD pattern of the geopolymer with 1.7 wt%  $\text{MgCl}_2 \cdot 6\text{H}_2\text{O}$  ( $G_{1.5-Cl_{1.7}}$ ) was the same as that of  $G_{1.5-0}$ . However, the geopolymers containing 8.5 wt%  $\text{MgCl}_2 \cdot 6\text{H}_2\text{O}$  contained halite ( $\text{NaCl}$ ), and with a further increase in the salt concentration, the peaks corresponding to halite intensified, indicating the formation of more halite, which was attributable to the combination of  $\text{Na}^+$  and  $\text{Cl}^-$  during the curing process. These results suggest that  $\text{Cl}^-$  more easily reacted with  $\text{Na}^+$  than  $\text{SO}_4^{2-}$  did because no crystal  $\text{Na}_2\text{SO}_4$  was detected.

### 3.2.2. FTIR Spectra

Figure 6 shows the FTIR spectra of selected geopolymers in the 400–1800  $\text{cm}^{-1}$  range. The FTIR spectra of  $G_0-0$  (Figure 6a) featured an absorption band at approximately 1648  $\text{cm}^{-1}$ , corresponding to the bending vibration of H–O–H, resulting from water absorption [57]. The broad band at approximately 1452  $\text{cm}^{-1}$  corresponded to the asymmetric stretching vibration of O–C–O from hydrotalcite-like phases,  $\text{Na}_2\text{CO}_3$ , and unreacted  $\text{CaCO}_3$  [55,58]. In addition, another band corresponding to the stretching vibration of carbonate from calcite occurred at 896  $\text{cm}^{-1}$  [55]. However, this band has been reported to correspond to the stretching vibration of Si–O from C-(A)-S-H [58]. Moreover, bands between 1200 and 900  $\text{cm}^{-1}$  corresponded to the asymmetric stretching vibration of Si–O–T (T: Si or Al); these bands, denoted as “main bands,” have been widely reported in research on the chemical properties of alkali-based geopolymers [59]. The small peak at 718  $\text{cm}^{-1}$  corresponded to Si–O–Al<sup>IV</sup> bending vibration, while those at 664 and 602  $\text{cm}^{-1}$  corresponded to deformation vibrations of Si–O–T from C-(A)-S-H [54]. Furthermore, the absorption bands at 483 and 456  $\text{cm}^{-1}$  corresponded to the bending vibration of Si–O–Si. After the addition of magnesium salts, the bands at 1452  $\text{cm}^{-1}$  shifted to a slightly higher field, which is attributable to the displacement of  $\text{CO}_3^{2-}$  and anions (i.e.,  $\text{Cl}^-$  and  $\text{SO}_4^{2-}$ ). The FTIR spectra featured no other change, indicating that the ions did not significantly alter the geopolymer molecular structure.

$G_{1.5-0}$  exhibited fewer and broader FTIR peaks than  $G_0-0$  (Figure 6b), indicating that a higher amount of amorphous phase was formed in  $\text{Na}_2\text{SiO}_3$ -activated GGBFS than in  $\text{NaOH}$ -activated GGBFS. In addition, the main band of  $G_{1.5-0}$  (969  $\text{cm}^{-1}$ ) was higher than that of  $G_0-0$  (953  $\text{cm}^{-1}$ ), demonstrating the incorporation of more Si in  $G_{1.5-0}$  than in  $G_0-0$  [60,61]. The FTIR spectra of the  $\text{NaOH}$ -activated GGBFS exhibited a band at approximately 876  $\text{cm}^{-1}$ , attributable to the presence of natural bond orbitals (e.g., Al–O<sup>−</sup>, Si–O<sup>−</sup>) resulting from the geopolymerization process [13]. The FTIR spectra of the magnesium-salt-containing geopolymers mainly differed from that of the salt-free GGBFS in the positions of the main bands; that is, the main band slightly shifted to a higher wavenumber after magnesium salt addition, attributable to the occurrence of more unreacted GGBFS owing to the reduced alkalinity resulting from the reaction between alkali and magnesium ions [62,63]. Consequently, the compressive strength decreased with increasing salt concentration. In addition, the absorption bands at approximately 619  $\text{cm}^{-1}$  in the  $G_{1.5-S_5}$  and  $G_{1.5-S_9}$  spectra could be attributed to the bending vibration of  $\text{SO}_4^{2-}$  [64]. Moreover, the band at 1104  $\text{cm}^{-1}$  in the  $G_{1.5-S_9}$  spectrum corresponded to the asymmetric stretching of  $\text{SO}_4^{2-}$  [65].



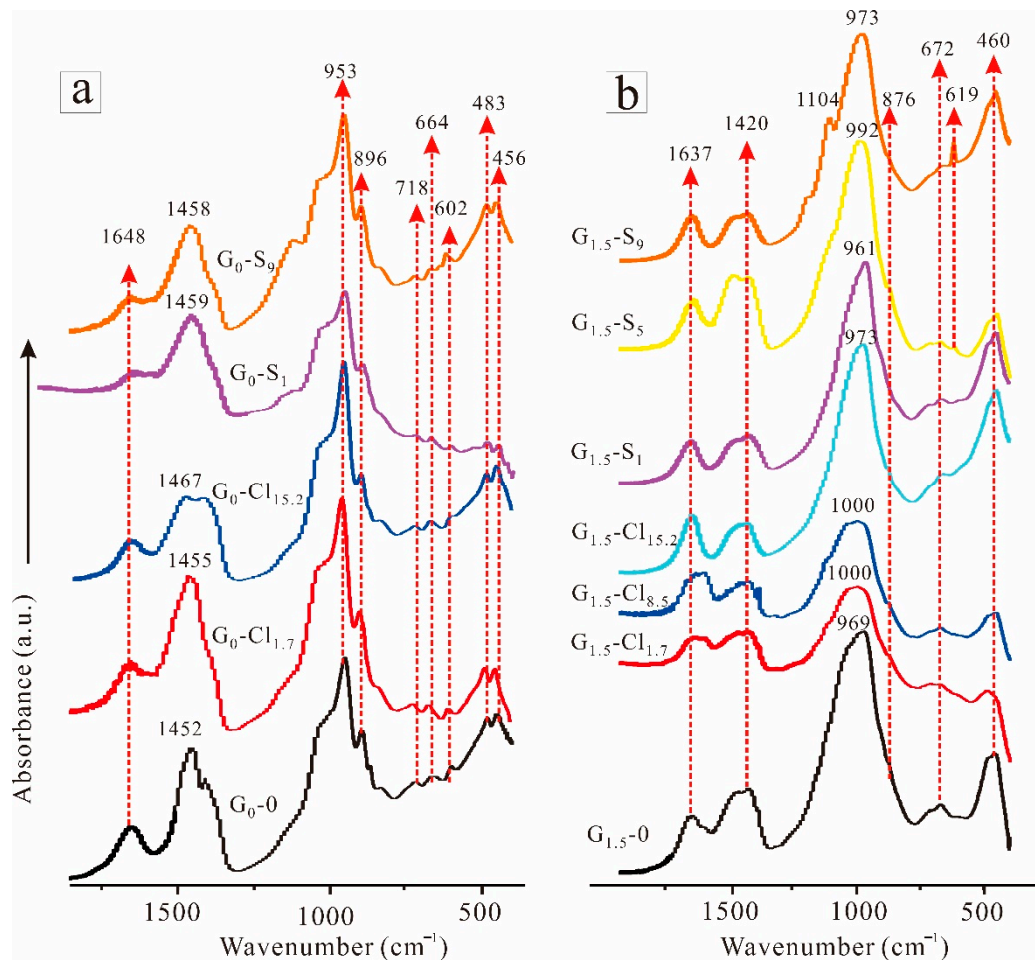


**Figure 6.** FTIR spectra of (a) NaOH-activated and (b)  $\text{Na}_2\text{SiO}_3$ -activated geopolymers.

### 3.2.3. TG Result

The thermal properties of  $G_0-0$ ,  $G_{1.5}-0$ ,  $G_{1.5}-\text{Cl}_{8.5}$ ,  $G_{1.5}-\text{Cl}_{15.2}$ , and  $G_{1.5}-\text{S}_9$  are shown in Figure 7.  $G_0-0$  exhibited a total mass loss of  $\sim 30\%$ , which was much greater than that of  $G_{1.5}-0$  ( $\sim 20\%$ ). The magnesium-salt-containing geopolymers exhibited a higher total mass loss, demonstrating that the salt restricted water evaporation from the geopolymeric paste. The Cl-containing geopolymers appeared to retain more water than the  $\text{SO}_4^{2-}$ -containing geopolymers because  $G_{1.5}-\text{Cl}_{8.5}$  and  $G_{1.5}-\text{Cl}_{15.2}$  exhibited a higher mass loss than  $G_{1.5}-\text{S}_9$  after calcination to  $900^\circ\text{C}$ .

The DSC curves of the geopolymers featured an endothermic peak ranging from  $30^\circ\text{C}$  to  $150^\circ\text{C}$ , attributable to the evaporation of free water and the decomposition of C-(A)-S-H gels [15]. Accordingly, considerable mass loss ( $>75\%$ ) occurred at this temperature range. The Cl-containing geopolymers exhibited the highest mass loss before  $150^\circ\text{C}$ , presumably because they retained the highest amount of free water. The continuous mass loss during calcination between  $150^\circ\text{C}$  and  $300^\circ\text{C}$  for all geopolymers can be attributed to the loss of bound water (interstitial water).  $G_0-0$  retained the most interstitial water [66]. Furthermore, the mass loss during calcination at  $300\text{--}600^\circ\text{C}$  was mainly due to the decomposition of hydroxyl water (dehydroxylation) [66]. The DSC curve of  $G_0-0$  featured a small endothermic peak, attributable to hydrocalcite decomposition; this peak was nonexistent in other samples [55]. These results substantiate the formation of hydrocalcite in NaOH-activated GGBFS-based geopolymers but not in  $\text{Na}_2\text{SiO}_4$ -activated geopolymers. Accordingly,  $G_0-0$  exhibited a higher mass loss than the other samples at  $300\text{--}600^\circ\text{C}$ . In addition, at temperatures exceeding  $600^\circ\text{C}$ , the geopolymers exhibited little change in mass loss, consistent with the findings of previous studies [4,67].

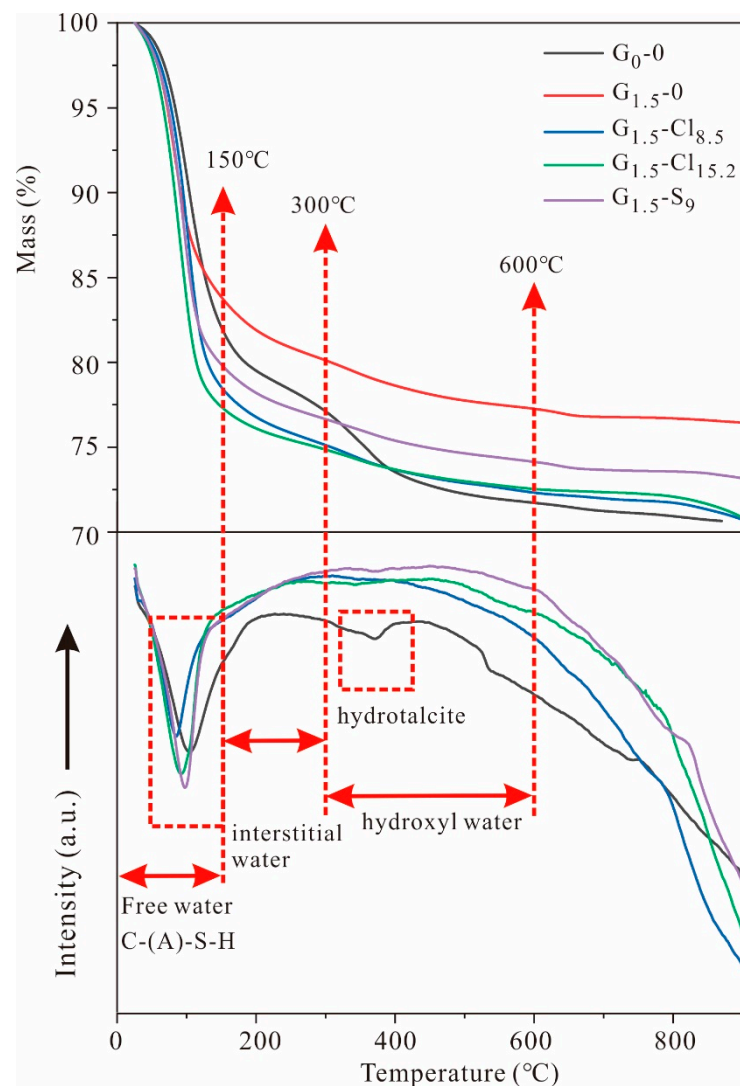


**Figure 7.** TG and DSC curves of selected geopolymers.

### 3.3. Microstructure of GGBFS-Based Geopolymers

#### 3.3.1. SEM/EDX Result

Figures 8–10 show the SEM images of selected geopolymers, and Figure 11 displays the EDX spectra of the red spots in Figures 8–10.  $G_0-0$  exhibited a compact microstructure but also had some cracks and macropores (Figure 8a). The gels were connected firmly, but many isolated particles still occurred, resulting in microstructure inhomogeneity. The EDX result (Figure 11, spot 1) indicated that the  $G_0-0$  matrix was mainly composed of O, Na, Ca, Si, and Al, indicating the formation of N,C-(A)-S-H gels and a strengthening effect. After the addition of magnesium salts, the geopolymer matrix became loosely bound, accompanied by the development of numerous cracks and pores (Figure 8c,e). However, the EDX results of  $G_0-Cl_{15.2}$  (Figure 11, spot 2) indicated that the  $Cl^-$  ions were not evenly distributed in the matrix. These results indicate that  $Cl^-$  may react with Na to form halite or displace  $CO_3^{2-}$  to form Cl-hydrotalcite, rather than spread in the matrix of the NaOH-activated, GGBFS-based geopolymer.  $G_0-S_9$  exhibited a similar result (Figure 11, spot 3); its S concentration was substantially less than that of  $G_{1.5}-S_9$  (Figure 11, spot 7). Although  $Mg^{2+}$  was also detected, GGBFS inherently contained some MgO; thus, it is difficult to determine the role of  $Mg^{2+}$ . In addition, some plate- and needle-like crystals occurred in  $G_0-Cl_{15.2}$  (Figure 8d); the plate-like crystals, owing to their hexagonal shape, could be Friedel's salt from the  $Cl^-$  content. Figure 8f shows that numerous large voids occurred in  $G_0-S_9$ , which reduced the ultimate compressive strength.

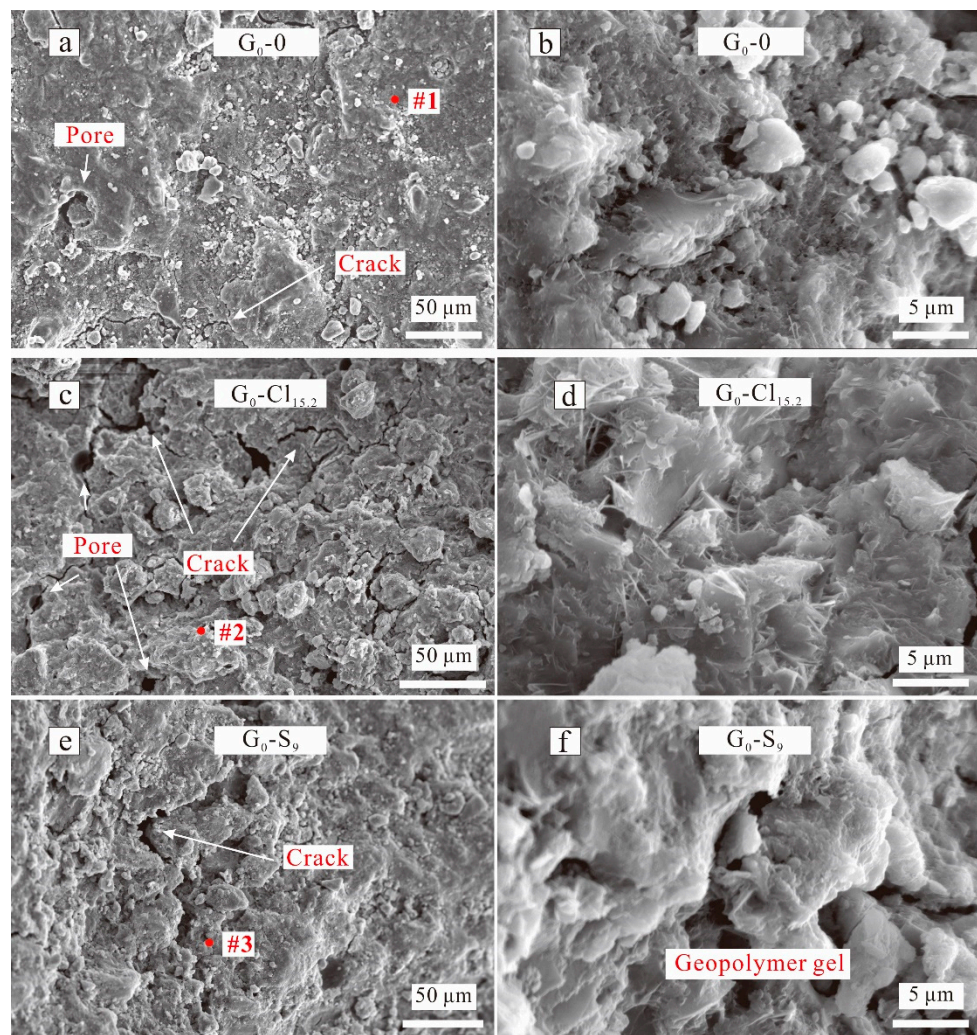


**Figure 8.** SEM images of NaOH-activated geopolymers of (a)  $G_0-0$ , (c)  $G_0-Cl_{15.2}$ , (e)  $G_0-S_9$  at low magnification; SEM images of NaOH-activated geopolymers of (b)  $G_0-0$ , (d)  $G_0-Cl_{15.2}$ , (f)  $G_0-S_9$  at high magnification.

Figure 9 displays the SEM images of  $G_{1.5}-0$ ,  $G_{1.5}-S_1$ , and  $G_{1.5}-S_9$ .  $G_{1.5}-0$  exhibited a considerably more compact morphology than  $G_0-0$ . Particularly,  $G_{1.6}-0$  exhibited a more homogeneous and denser matrix than  $G_0-0$  (Figures 8b and 9b), corresponding to a higher compressive strength. However, numerous microcracks occurred in the matrix. Numerous microcracks also occurred in  $G_{1.5}-S_1$  and  $G_{1.5}-Cl_9$  (Figure 9d,f). The EDX results showed that the  $G_{1.6}-0$  matrix (Figure 11, spot 4) also contained O, Na, Ca, Si, and Al to form N,C-(A)-S-H gels. In addition,  $G_{1.5}-0$  exhibited a higher Si concentration than  $G_0-0$ , which was also related to the higher compressive strength of  $G_{1.5}-0$  than  $G_0-0$  [53]. Furthermore, the homogeneous-matrix geopolymer exhibited higher Ca and Si concentrations (Figure 11, spot 5) than the geopolymer with a less homogeneous matrix (Figure 11, spot 4), which substantiates the important roles of Ca and Si in the geopolymer matrix densification.

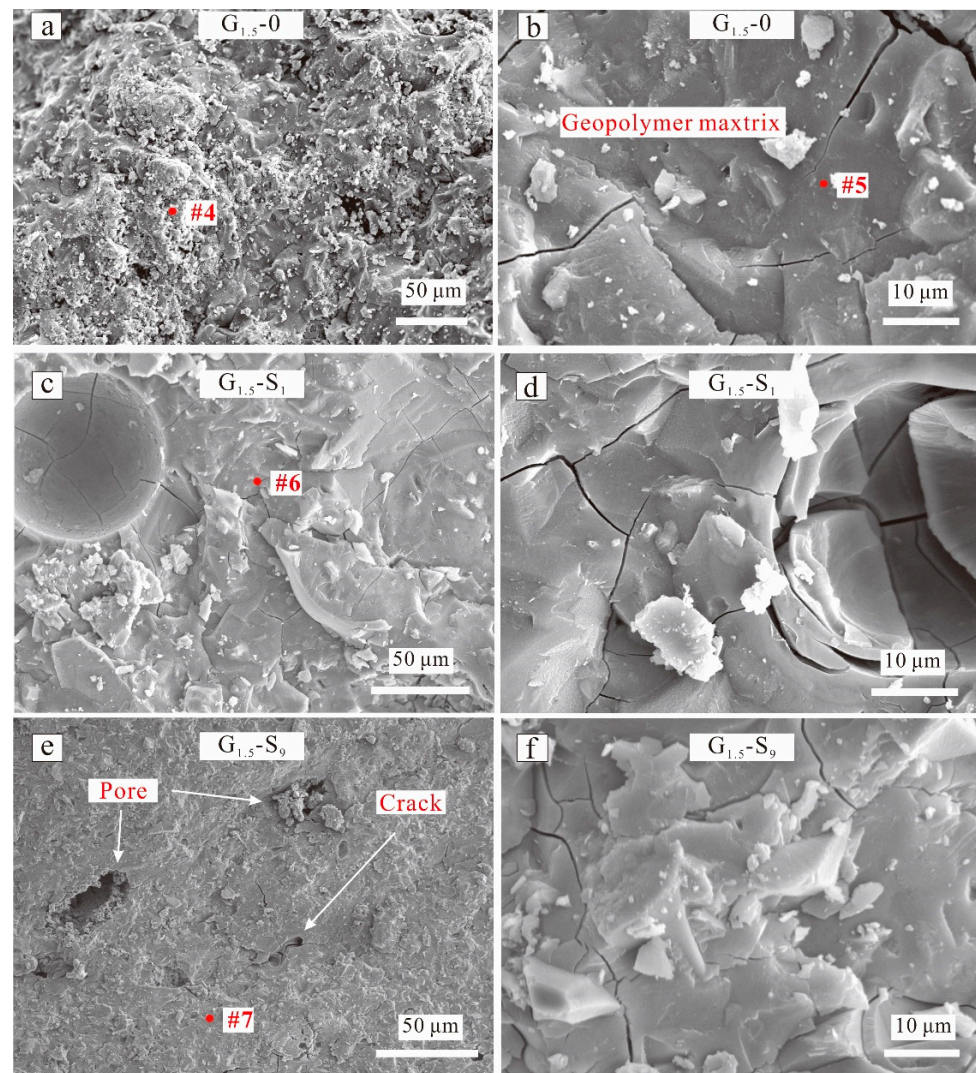


**Figure 9.** SEM images of  $\text{Na}_2\text{SiO}_4$ -activated geopolymers of (a)  $G_{1.5-0}$ , (c)  $G_{1.5-S_1}$ , (e)  $G_{1.5-S_9}$  at low magnification; SEM images of  $\text{Na}_2\text{SiO}_4$ -activated geopolymers of (b)  $G_{1.5-0}$ , (d)  $G_{1.5-S_1}$ , (f)  $G_{1.5-S_9}$  at high magnification.

The morphologies of the  $\text{MgSO}_4$ -containing geopolymers were not considerably different from that of the  $\text{MgSO}_4$ -free geopolymer.  $G_{1.5-S_1}$  exhibited a relatively compact and dense morphology (Figure 9c,e) but contained numerous microcracks (Figure 9d,f). In addition, the geopolymer matrix contained numerous macropores, which originated from the entrapped air. The S concentration of the  $\text{MgSO}_4$ -containing geopolymers, detected via EDX spectroscopy, increased with increasing  $\text{MgSO}_4$  concentration (Figure 11, spots 6, 7), indicating that  $\text{SO}_4^{2-}$  was evenly distributed in the geopolymer matrix. However, the  $\text{Mg}^{2+}$  concentration did not change in this manner.

Figure 10 shows the SEM images of  $G_{1.5-Cl}$ .  $G_{1.5-Cl_{1.7}}$ , which exhibited a dense microstructure (Figure 10a) and showed no morphological difference from  $G_{1.5-0}$ . Only a little amount of Cl element was detected via EDX spectroscopy (Figure 11, spot 8). The geopolymer with a salt concentration of 8.5 wt% exhibited a loosely bound matrix, macrocracks, uneven surface, and an inhomogeneous microstructure (Figure 10c), and numerous particles were distributed on the surface of the geopolymer matrix (Figure 10d).  $G_{1.5-Cl_{15.2}}$  exhibited a more compact matrix than  $G_{1.5-Cl_{8.5}}$  (Figure 10e), indicating that increasing the curing temperature favored the densification of the geopolymer matrix. However, numerous pores and particles occurred on the matrix surface. All of these changes in the microstructure reduced compressive strength.

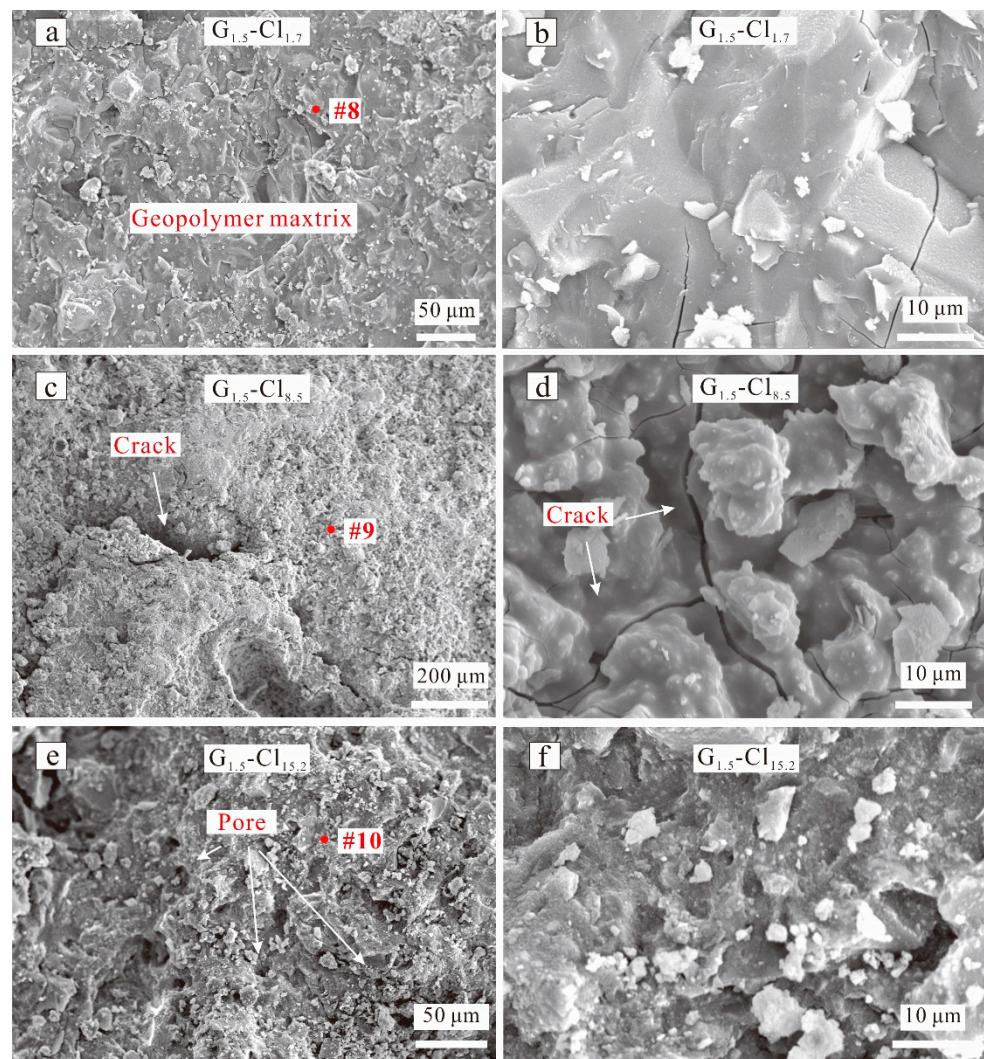


**Figure 10.** SEM images of  $\text{Na}_2\text{SiO}_4$ -activated geopolymers of (a)  $\text{G}_{1.5}\text{-Cl}_{1.7}$ , (c)  $\text{G}_{1.5}\text{-Cl}_{8.5}$ , (e)  $\text{G}_{1.5}\text{-Cl}_{15.2}$  at low magnification; SEM images of  $\text{Na}_2\text{SiO}_4$ -activated geopolymers of (b)  $\text{G}_{1.5}\text{-Cl}_{1.7}$ , (d)  $\text{G}_{1.5}\text{-Cl}_{8.5}$ , (f)  $\text{G}_{1.5}\text{-Cl}_{15.2}$  at high magnification.

The EDX result showed that  $\text{Cl}^-$  was evenly distributed in the matrix (Figure 11, spots 9, 10). With increasing  $\text{MgCl}_2 \cdot 6\text{H}_2\text{O}$  concentration, the Cl content increased, while the Ca concentration decreased and the Na concentration gradually increased, suggesting that  $\text{Cl}^-$  enhanced N-A-S-H gel formation.

### 3.3.2. MIP Result

Figure 12 displays the pore size distribution and cumulative intrusion curve of GGBFS-based geopolymers, and Table 1 shows the pore parameters of the geopolymers. Pore structure is a major parameter influencing the mechanical properties of geopolymers. Wu et al. [68] categorized pores in cement into three groups according to pore size: gel pores (<10 nm), capillary pores (10–5000 nm), and macropores (>5000 nm).

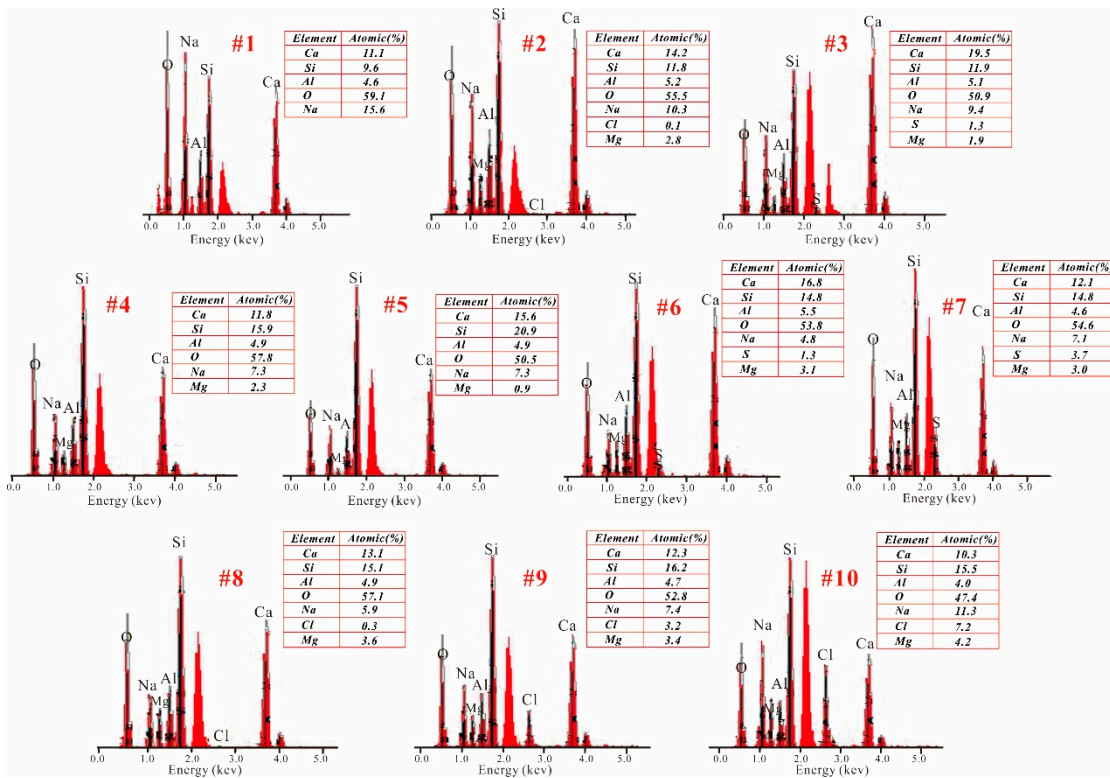


Figure 11. EDX spectra of geopolymers. (The number indicated the red spots in Figures 8–10).

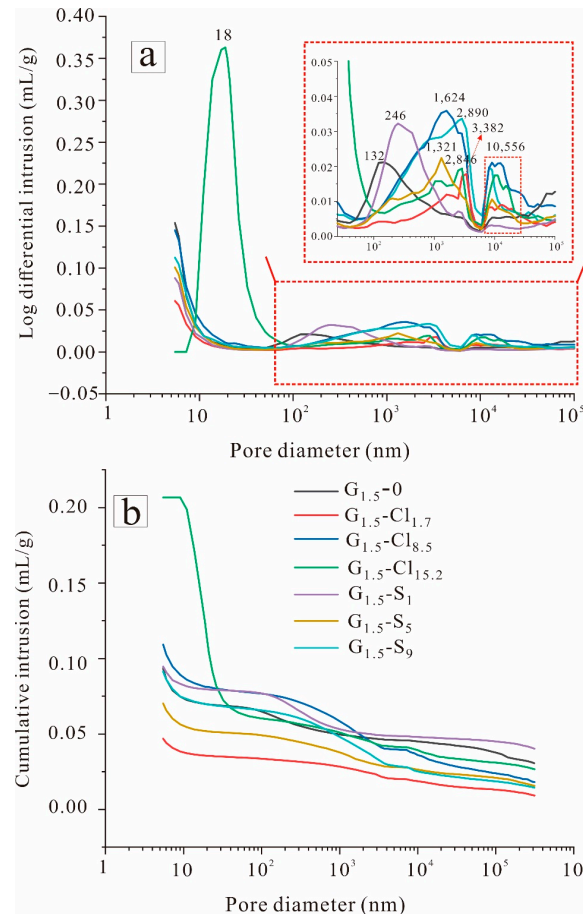


Figure 12. MIP results of geopolymers: (a) log differential intrusion and (b) cumulative intrusion.

**Table 1.** Geopolymer pore parameters based on MIP results.

Samples	Total Pore Area (m <sup>2</sup> /g)	Average Pore Diameter (nm)	Porosity (%)
G <sub>1.5</sub> -0	13.85	26.97	15.81
G <sub>1.5</sub> -Cl <sub>1.7</sub>	6.33	29.65	8.03
G <sub>1.5</sub> -Cl <sub>8.5</sub>	15.48	28.22	16.13
G <sub>1.5</sub> -Cl <sub>18.2</sub>	34.11	24.23	29.25
G <sub>1.5</sub> -S <sub>1</sub>	8.88	42.68	15.41
G <sub>1.5</sub> -S <sub>5</sub>	10.33	27.20	11.51
G <sub>1.5</sub> -S <sub>9</sub>	12.23	29.87	14.45

Figure 12a illustrates the critical pore sizes of the salt-free and salt-containing Na<sub>2</sub>SiO<sub>4</sub>-activated geopolymers. G<sub>1.5</sub>-0 mostly exhibited capillary pores of ~132 nm. The MgCl<sub>2</sub>·6H<sub>2</sub>O-containing geopolymers exhibited larger capillary pores, as indicated by the higher peaks, and macropores of ~10,556 nm. These results demonstrate that MgCl<sub>2</sub>·6H<sub>2</sub>O enlarged the geopolymer pore structure. In addition, with increasing MgCl<sub>2</sub>·6H<sub>2</sub>O concentration, the total pore area of G<sub>1.5</sub>-Cl increased, and the average pore diameter gradually decreased (Table 1). G<sub>1.5</sub>-Cl<sub>15.2</sub> exhibited few capillary pores of ~18 nm, as indicated by the sharp peak, attributable to halite formation. Figure 12b indicates that MgCl<sub>2</sub>·6H<sub>2</sub>O addition increased the geopolymer pore volume, except for G<sub>1.5</sub>-Cl<sub>1.7</sub>, consistent with the total pore area results (Table 1). Moreover, the porosity of G<sub>1.5</sub>-Cl increased with increasing MgCl<sub>2</sub>·6H<sub>2</sub>O concentration. Therefore, high MgCl<sub>2</sub>·6H<sub>2</sub>O concentrations deteriorate the pore structure of the geopolymer and thus its compressive strength.

MgSO<sub>4</sub> addition also increased the critical pore size of the geopolymer. As the MgSO<sub>4</sub> concentration increased from 0 to 9.0 wt%, the capillary pore size gradually increased from 132 to 2846 nm, and macropores progressively developed, as indicated by the corresponding more intense and broader peaks. Therefore, salt addition favored macropore production in the geopolymer. Studies have shown that pores of 10 to 1000 nm may be harmful to the mechanical properties of cement [69]. With increasing critical pore size, compressive strength reduced. Compared with G<sub>1.5</sub>-0, G<sub>1.5</sub>-S<sub>5</sub> exhibited a lower pore volume, while G<sub>1.5</sub>-S<sub>9</sub> exhibited basically the same pore volume, different from the case of G<sub>1.5</sub>-Cl. This was also evidenced by the geopolymer porosity values (Table 1). These results demonstrate that different ions had different effects on the geopolymer pore structure, attributable to the formation of different products. However, the related influence mechanism remains unclear, which necessitates further study. Although the pore volume decreased, the compressive strength also decreased, presumably because some pores were filled with SO<sub>4</sub><sup>2-</sup>-containing precipitation and thus did not contribute to strength.

### 3.4. Summary and Final Discussion

This study found that both MgSO<sub>4</sub> and MgCl<sub>2</sub> negatively affected the microstructure and compressive strength of alkali-activated, GGBFS-based geopolymers but did not considerably affect the chemical composition. For example, the addition of 10 wt% MgSO<sub>4</sub> did not alter the XRD patterns of G<sub>1.5</sub>-0 but reduced the 28 d compressive strength by 32.7%, while the addition of 8.5 wt% MgCl<sub>2</sub> resulted in the formation of only halite in the geopolymer but reduced the 28 d compressive strength by 51.5%. These results are consistent with those of previous studies. Lee et al. [47] studied the effect of inorganic salt on the compressive strength of kaolin/FA-based geopolymer. The 270 d compressive strengths decreased from 65.6 MPa to 24.9, 18.4, and 12.2 MPa after the addition of 0.08 moles of KCl, CaCl<sub>2</sub>, and MgCl<sub>2</sub>, respectively. Criado et al. [48] investigated the effect of Na<sub>2</sub>SO<sub>4</sub> on the alkali activation of an FA-based geopolymer and found that Na<sub>2</sub>SO<sub>4</sub> addition reduced the 180 d compressive strength of the geopolymer from 78.0 to 40.5 MPa; they attributed this decrease to the drop in the N-A-S-H concentration after Na<sub>2</sub>SO<sub>4</sub> addition.

However, in the current study, magnesium salt addition resulted in a more significant reduction in early compressive strength than late compressive strength. In contrast, previous studies on seawater-mixed geopolymers have shown that the ions in seawater

significantly increase the early compressive strength of the geopolymer. Ren et al. [48] observed that the 1 d compressive strength of seawater-mixed, slag-based geopolymer was 27.2 MPa, slightly greater than that of the distilled-water-mixed geopolymer (23.6 MPa). Lv et al. [70] reported that one-part alkali-activated GGBFS-FA mixed with tap water and seawater exhibited comparable flexural and compressive strengths. However, the seawater-mixed geopolymer showed slightly higher early strengths (1 and 14 days) than the tap-water-mixed geopolymer. Kang et al. [71] reported that compared with tap water, seawater as mixing water reduced the large- and medium-sized pores and increased the gel pores of slag-based geopolymers; therefore, the seawater-mixed geopolymer showed higher 3 d compressive strength than the tap-water-mixed geopolymer. The discrepancy between the effects of salt ions between the current study and previous studies is attributable to the presence of multiple salts in seawater compared with the sole salt in this study; nonetheless, further study on this discrepancy is warranted.

This study revealed that the microstructure and mechanical properties of GGBFS-based geopolymers were remarkably influenced by magnesium salt. The findings have several implications for the application of alkali-activated, GGBFS-based geopolymers. For example, considering that Cl exhibited a more pronounced negative effect than  $\text{SO}_4$ , practitioners should pay more attention to Cl during the preparation of GGBFS-based geopolymers with seawater or ion-contaminated water. In addition, the ions more significantly reduced the early mechanical properties than the late mechanical properties (Figure 4). Therefore, ion-contaminated, GGBFS-based geopolymers should be sufficiently cured to achieve high strength before application in infrastructure construction or composite manufacturing. Moreover, the ions present in the geopolymers can retain water (Figure 7), reducing the geopolymer's propensity to shrink. The water retention property must be carefully considered before the application of ion-contaminated, GGBFS-based geopolymers in some dry areas to prevent the significant loss of water.

Some limitations also need to be considered. First, the leaching behavior of  $\text{Mg}^{2+}$ ,  $\text{Cl}^-$ , and  $\text{SO}_4^{2-}$  was not well established in the literature, and the solidification ability of ions for ion-contaminated, GGBFS-based geopolymers is vital to their applicability. For example, free  $\text{Cl}^-$  can initiate rebar corrosion; thus, materials with reduced free  $\text{Cl}^-$  are beneficial for rebar construction [72]. Second, geopolymer durability was not investigated in this study. Good durability, which is related to high anti-chloride penetration, anti-sulfate attack, and anti-carbonation, is essential in applications in marine environments [73]. Lastly, this study only investigated the composition, microstructure, and compressive strength of ion-contaminated mixed geopolymers aged for up to 28 days. With increasing aging time, the mineral composition and mechanical properties may significantly change. Burciaga-Díaz et al. [55] found that a NaOH-activated, slag/metakaolin-based geopolymer transitioned from an amorphous phase into a well-ordered phase over 6 years, with corresponding changes in physical and chemical properties. Therefore, the long-term properties of the investigated geopolymers need to be further explored.

#### 4. Conclusions

In this study, through spectroscopic and microscopic techniques, we investigated the effects of magnesium salts, the main ion content of seawater, on the compressive strength and microstructure of as-obtained, GGBFS-based geopolymers.

The activation of GGBFS with NaOH resulted in the formation of C-(A)-S-H crystals, C-(A)-S-H gels, hydrotalcite-like phases, and chlormagaluminite. The addition of  $\text{MgCl}_2 \cdot 6\text{H}_2\text{O}$  or  $\text{MgSO}_4$  loosened the microstructure of the geopolymer, thereby reducing its compressive strength. With increasing salt concentration, the compressive strength gradually decreased.  $\text{MgCl}_2 \cdot 6\text{H}_2\text{O}$  addition induced the formation of halite and Cl-hydrotalcite, whereas  $\text{MgSO}_4$  addition did not significantly alter the mineral phase and morphology of the geopolymer.

The activation of GGBFS with  $\text{Na}_2\text{SiO}_3$  mainly produced C-(A)-S-H crystal and amorphous C-(A)-S-H gels. The anions ( $\text{Cl}^-$ ,  $\text{SO}_4^{2-}$ ) were evenly distributed in the geopolymer



matrix after magnesium salt addition. With increasing magnesium salt concentration, the critical pore size of the geopolymer increased, the microstructure became less compact and loosely bound, and thus the compressive strength gradually decreased.  $\text{MgCl}_2 \cdot 6\text{H}_2\text{O}$  addition induced halite formation and increased the geopolymer pore volume, whereas  $\text{MgSO}_4$  addition did not significantly alter the mineral phase and pore volume of the geopolymer.

Further research into the durability and long-term properties of seawater-mixed, GGBFS-based geopolymers, the role of Mg ions, and the role of other salts is still required to elucidate the practical applicability of the geopolymers.

**Author Contributions:** Data curation, K.Z., Y.L., L.L. and Z.X.; investigation, K.Z., K.W., B.Z. and D.L.; methodology, K.W., Z.L., Z.Y., B.Z. and Y.L.; resources, Z.L. and Z.Y.; supervision, D.L. and L.L.; validation, D.L.; visualization, Z.Y. and Z.X.; writing—original draft, K.Z.; writing—review and editing, K.W., B.Z. and L.L. All authors have read and agreed to the published version of the manuscript.

**Funding:** This research was funded by the National Natural Science Foundation of China under Grant No. 12032009 and No. 12002091.

**Conflicts of Interest:** The authors declare no conflict of interest.

## References

1. Koleyński, A.; Król, M.; Ychowicz, M. The structure of geopolymers—Theoretical studies. *J. Mol. Struct.* **2018**, *1163*, 465–471. [[CrossRef](#)]
2. Davidovits, J. *Geopolymer Chemistry and Applications*; Institut Géopolymère: Saint-Quentin, France, 2011.
3. Valentini, L. Modeling Dissolution–Precipitation Kinetics of Alkali-Activated Metakaolin. *ACS Omega* **2018**, *3*, 18100–18108. [[CrossRef](#)] [[PubMed](#)]
4. Zhang, B.; Yuan, P.; Guo, H.; Deng, L.; Li, Y.; Li, L.; Wang, Q.; Liu, D. Effect of curing conditions on the microstructure and mechanical performance of geopolymers derived from nanosized tubular halloysite. *Constr. Build. Mater.* **2020**, *268*, 121186. [[CrossRef](#)]
5. Amran, Y.M.; Alyousef, R.; Alabduljabbar, H.; El-Zeadani, M. Clean production and properties of geopolymer concrete. A review. *J. Clean. Prod.* **2019**, *251*, 119679. [[CrossRef](#)]
6. Zhu, H.; Liang, G.; Li, H.; Wu, Q.; Zhang, C.; Yin, Z.; Hua, S. Insights to the sulfate resistance and microstructures of alkali-activated metakaolin/slag pastes. *Appl. Clay Sci.* **2021**, *202*, 105968. [[CrossRef](#)]
7. Ji, Z.; Pei, Y. Bibliographic and visualized analysis of geopolymer research and its application in heavy metal immobilization: A review. *J. Environ. Manag.* **2018**, *231*, 256–267. [[CrossRef](#)]
8. Walkley, B.; Ke, X.; Hussein, O.H.; Bernal, S.A.; Provis, J.L. Incorporation of strontium and calcium in geopolymer gels. *J. Hazard. Mater.* **2019**, *382*, 121015. [[CrossRef](#)]
9. Lee, N.K.; Khalid, H.R.; Lee, H.K. Adsorption characteristics of cesium onto mesoporous geopolymers containing nano-crystalline zeolites. *Microporous Mesoporous Mater.* **2017**, *242*, 238–244. [[CrossRef](#)]
10. Duxson, P.; Provis, J.L.; Lukey, G.C.; Deventer, J.S.J.V. The role of inorganic polymer technology in the development of ‘green concrete’. *Cem. Concr. Res.* **2007**, *37*, 1590–1597. [[CrossRef](#)]
11. Turner, L.K.; Collins, F.G. Carbon dioxide equivalent ( $\text{CO}_2\text{-e}$ ) emissions: A comparison between geopolymer and OPC cement concrete. *Constr. Build. Mater.* **2013**, *43*, 125–130. [[CrossRef](#)]
12. McLellan, B.C.; Williams, R.P.; Lay, J.; van Riessen, A.; Corder, G.D. Costs and carbon emissions for geopolymer pastes in comparison to ordinary portland cement. *J. Clean. Prod.* **2011**, *19*, 1080–1090. [[CrossRef](#)]
13. Zhang, B.; Guo, H.; Yuan, P.; Li, Y.; Wang, Q.; Deng, L.; Liu, D. Geopolymerization of halloysite via alkali-activation: Dependence of microstructures on precalcination. *Appl. Clay Sci.* **2019**, *185*, 105375. [[CrossRef](#)]
14. Sgarlata, C.; Formia, A.; Siligardi, C.; Ferrari, F.; Leonelli, C. Mine Clay Washing Residues as a Source for Alkali-Activated Binders. *Materials* **2021**, *15*, 83. [[CrossRef](#)] [[PubMed](#)]
15. Wang, Q.; Guo, H.; Yu, T.; Yuan, P.; Deng, L.; Zhang, B. Utilization of Calcium Carbide Residue as Solid Alkali for Preparing Fly Ash-Based Geopolymers: Dependence of Compressive Strength and Microstructure on Calcium Carbide Residue, Water Content and Curing Temperature. *Materials* **2022**, *15*, 973. [[CrossRef](#)] [[PubMed](#)]
16. Yang, J.; Xu, L.; Wu, H.; Jin, J.; Liu, L. Microstructure and mechanical properties of metakaolin-based geopolymer composites containing high volume of spodumene tailings. *Appl. Clay Sci.* **2022**, *218*, 106412. [[CrossRef](#)]
17. Hu, S.; Zhong, L.; Yang, X.; Bai, H.; Ren, B.; Zhao, Y.; Zhang, W.; Ju, X.; Wen, H.; Mao, S.; et al. Synthesis of rare earth tailing-based geopolymer for efficiently immobilizing heavy metals. *Constr. Build. Mater.* **2020**, *254*, 119273. [[CrossRef](#)]
18. Xu, H.; Deventer, J.S.J.V. Geopolymerisation of multiple minerals. *Miner. Eng.* **2002**, *15*, 1131–1139. [[CrossRef](#)]
19. Elmahdoubi, F.; Mabroum, S.; Hakkou, R.; Ibnoussina, M. Geopolymer Materials Based on Natural Pozzolans from the Moroccan Middle Atlas. *Minerals* **2021**, *11*, 1344. [[CrossRef](#)]

20. Maruthupandian, S.; Chaliasou, A.; Kanellopoulos, A. Recycling mine tailings as precursors for cementitious binders—Methods, challenges and future outlook. *Constr. Build. Mater.* **2021**, *312*, 125333.
21. Zhao, X.; Liu, C.; Zuo, L.; Wang, L.; Zhu, Q.; Liu, Y.; Zhou, B. Synthesis and characterization of fly ash geopolymer paste for goaf backfill: Reuse of soda residue. *J. Clean. Prod.* **2020**, *260*, 121045. [[CrossRef](#)]
22. Ye, N.; Chen, Y.; Yang, J.; Liang, S.; Hu, Y.; Xiao, B.; Huang, Q.; Shi, Y.; Hu, J.; Wu, X. Co-disposal of MSWI fly ash and Bayer red mud using an one-part geopolymeric system. *J. Hazard. Mater.* **2016**, *318*, 70–78. [[CrossRef](#)] [[PubMed](#)]
23. Zhang, B.; Feng, Y.; Xie, J.; Lai, D.; Yu, T.; Huang, D. Rubberized geopolymer concrete: Dependence of mechanical properties and freeze-thaw resistance on replacement ratio of crumb rubber. *Constr. Build. Mater.* **2021**, *310*, 125248. [[CrossRef](#)]
24. Abdila, S.R.; Abdullah, M.M.A.B.; Ahmad, R.; Nergis, D.D.B.; Rahim, S.Z.A.; Omar, M.F.; Sandu, A.V.; Vizureanu, P. Syafwandi Potential of Soil Stabilization Using Ground Granulated Blast Furnace Slag (GGBFS) and Fly Ash via Geopolymerization Method: A Review. *Materials* **2022**, *15*, 375. [[CrossRef](#)] [[PubMed](#)]
25. Jamari, J.; Ammarullah, M.I.; Santoso, G.; Sugiharto, S.; Supriyono, T.; Prakoso, A.T.; Basri, H.; van der Heide, E. Computational Contact Pressure Prediction of CoCrMo, SS 316L and Ti6Al4V Femoral Head against UHMWPE Acetabular Cup under Gait Cycle. *J. Funct. Biomater.* **2022**, *13*, 64. [[CrossRef](#)] [[PubMed](#)]
26. Xie, J.; Wang, J.; Rao, R.; Wang, C.; Fang, C. Effects of combined usage of GGBS and fly ash on workability and mechanical properties of alkali activated geopolymer concrete with recycled aggregate. *Compos. Part B Eng.* **2018**, *164*, 179–190. [[CrossRef](#)]
27. Lao, J.-C.; Xu, L.-Y.; Huang, B.-T.; Dai, J.-G.; Shah, S.P. Strain-hardening Ultra-High-Performance Geopolymer Concrete (UHPGC): Matrix design and effect of steel fibers. *Compos. Commun.* **2022**, *30*, 101081. [[CrossRef](#)]
28. Tembhurkar, S.; Ralegaonkar, R.; Azevedo, A.; Madurwar, M. Low cost geopolymer modular toilet unit for ODF India—A case study. *Case Stud. Constr. Mater.* **2022**, *16*. [[CrossRef](#)]
29. Gu, G.; Ma, T.; Chen, F.; Xu, F.; Zhang, J. Electromagnetic and mechanical properties of FA-GGBFS geopolymer composite used for induction heating of airport pavement. *Cem. Concr. Compos.* **2022**, *129*, 104503. [[CrossRef](#)]
30. Miller, S.A.; Horvath, A.; Monteiro, P.J.M. Impacts of booming concrete production on water resources worldwide. *Nat. Sustain.* **2018**, *1*, 69–76. [[CrossRef](#)]
31. Heravi, G.; Abdolvand, M.M. Assessment of water consumption during production of material and construction phases of residential building projects. *Sustain. Cities Soc.* **2019**, *51*, 101785. [[CrossRef](#)]
32. Xiong, Z.; Mai, G.; Qiao, S.; He, S.; Zhang, B.; Wang, H.; Zhou, K.; Li, L. Fatigue bond behaviour between basalt fibre-reinforced polymer bars and seawater sea-sand concrete. *Ocean Coast. Manag.* **2022**, *218*, 106038. [[CrossRef](#)]
33. Huang, Y.; Qi, X.; Li, C.; Gao, P.; Wang, Z.; Ying, J. Seismic behaviour of seawater coral aggregate concrete columns reinforced with epoxy-coated bars. *Structures* **2021**, *36*, 822–836. [[CrossRef](#)]
34. Zhang, B.; Zhu, H.; Cao, R.; Ding, J.; Chen, X. Feasibility of using geopolymers to investigate the bond behavior of FRP bars in seawater sea-sand concrete. *Constr. Build. Mater.* **2021**, *282*, 122636. [[CrossRef](#)]
35. Wang, J.; Liu, E.; Li, L. Multiscale investigations on hydration mechanisms in seawater OPC paste. *Constr. Build. Mater.* **2018**, *191*, 891–903. [[CrossRef](#)]
36. Rashad, A.M.; Ezzat, M. A Preliminary study on the use of magnetic, Zamzam, and sea water as mixing water for alkali-activated slag pastes. *Constr. Build. Mater.* **2019**, *207*, 672–678. [[CrossRef](#)]
37. Jun, Y.; Bae, Y.H.; Shin, T.Y.; Kim, J.H.; Yim, H.J. Alkali-Activated Slag Paste with Different Mixing Water: A Comparison Study of Early-Age Paste Using Electrical Resistivity. *Materials* **2020**, *13*, 2447. [[CrossRef](#)]
38. Jun, Y.; Yoon, S.; Oh, J.E. A Comparison Study for Chloride-Binding Capacity between Alkali-Activated Fly Ash and Slag in the Use of Seawater. *Appl. Sci.* **2017**, *7*, 971. [[CrossRef](#)]
39. Sabzi, M.; Far, S.M.; Dezfuli, S.M. Effect of melting temperature on microstructural evolutions, behavior and corrosion morphology of Hadfield austenitic manganese steel in the casting process. *Int. J. Miner. Met. Mater.* **2018**, *25*, 1431–1438. [[CrossRef](#)]
40. Mousavi Anijdan, S.H.; Sabzi, M. The effect of pouring temperature and surface angle of vortex casting on microstructural changes and mechanical properties of 7050Al-3 wt% SiC composite. *Mater. Sci. Eng. A Struct.* **2018**, *737*, 230–235. [[CrossRef](#)]
41. Nassajpour-Esfahani, A.H.; Bahrami, A.; Alhaji, A.; Emadi, R. Optimization of slip casting parameters for spark plasma sintering of transparent MgAl<sub>2</sub>O<sub>4</sub>/Si<sub>3</sub>N<sub>4</sub> nanocomposite. *Ceram. Int.* **2019**, *45*, 20714–20723. [[CrossRef](#)]
42. Ren, J.; Sun, H.; Cao, K.; Ren, Z.; Zhou, B.; Wu, W.; Xing, F. Effects of natural seawater mixing on the properties of alkali-activated slag binders. *Constr. Build. Mater.* **2021**, *294*, 123601. [[CrossRef](#)]
43. Jun, Y.; Kim, T.; Kim, J.H. Chloride-bearing characteristics of alkali-activated slag mixed with seawater: Effect of different salinity levels. *Cem. Concr. Compos.* **2020**, *112*, 103680. [[CrossRef](#)]
44. Siddique, S.; Jang, J.G. Mechanical Properties, Microstructure, and Chloride Content of Alkali-Activated Fly Ash Paste Made with Sea Water. *Materials* **2020**, *13*, 1467. [[CrossRef](#)] [[PubMed](#)]
45. Xiao, J.; Xu, Z.; Murong, Y.; Wang, L.; Lei, B.; Chu, L.; Jiang, H.; Qu, W. Effect of Chemical Composition of Fine Aggregate on the Frictional Behavior of Concrete–Soil Interface under Sulfuric Acid Environment. *Fractal Fract.* **2021**, *6*, 22. [[CrossRef](#)]
46. Wang, A.; Zheng, Y.; Zhang, Z.; Liu, K.; Li, Y.; Shi, L.; Sun, D. The Durability of Alkali-Activated Materials in Comparison with Ordinary Portland Cements and Concretes: A Review. *Engineering* **2020**, *6*, 695–706. [[CrossRef](#)]
47. Lee, W.; van Deventer, J. The effects of inorganic salt contamination on the strength and durability of geopolymers. *Colloids Surf. A Physicochem. Eng. Asp.* **2002**, *211*, 115–126. [[CrossRef](#)]

48. Criado, M.; Jimenez, A.M.F.; Palomo, A. Effect of sodium sulfate on the alkali activation of fly ash. *Cem. Concr. Compos.* **2010**, *32*, 589–594. [[CrossRef](#)]
49. Lv, Q.-F.; Wang, Z.-S.; Gu, L.-Y.; Chen, Y.; Shan, X.-K. Effect of sodium sulfate on strength and microstructure of alkali-activated fly ash based geopolymer. *J. Cent. South Univ.* **2020**, *27*, 1691–1702. [[CrossRef](#)]
50. Brough, A.; Holloway, M.; Sykes, J.; Atkinson, A. Sodium silicate-based alkali-activated slag mortars: Part II. The retarding effect of additions of sodium chloride or malic acid. *Cem. Concr. Res.* **2000**, *30*, 1375–1379. [[CrossRef](#)]
51. Rattanasak, U.; Pankhet, K.; Chindaprasirt, P. Effect of chemical admixtures on properties of high-calcium fly ash geopolymer. *Int. J. Miner. Met. Mater.* **2011**, *18*, 364–369. [[CrossRef](#)]
52. Longhi, M.A.; Walkley, B.; Rodríguez, E.D.; Kirchheim, A.P.; Zhang, Z.; Wang, H. New selective dissolution process to quantify reaction extent and product stability in metakaolin-based geopolymers. *Compos. Part B Eng.* **2019**, *176*, 107172. [[CrossRef](#)]
53. He, P.; Wang, M.; Fu, S.; Jia, D.; Yan, S.; Yuan, J.; Xu, J.; Wang, P.; Zhou, Y. Effects of Si/Al ratio on the structure and properties of metakaolin based geopolymer. *Ceram. Int.* **2016**, *42*, 14416–14422. [[CrossRef](#)]
54. Kapeluszna, E.; Kotwica, Ł.; Różycka, A.; Gołek, Ł. Incorporation of Al in C-A-S-H gels with various Ca/Si and Al/Si ratio: Microstructural and structural characteristics with DTA/TG, XRD, FTIR and TEM analysis. *Constr. Build. Mater.* **2017**, *155*, 643–653. [[CrossRef](#)]
55. Burciaga-Díaz, O.; Escalante-García, J.I. Structural transition to well-ordered phases of NaOH-activated slag-metakaolin cements aged by 6 years. *Cem. Concr. Res.* **2022**, *156*, 106791. [[CrossRef](#)]
56. Khan, M.; Kayali, O.; Troitzsch, U. Effect of NaOH activation on sulphate resistance of GGBFS and binary blend pastes. *Cem. Concr. Compos.* **2017**, *81*, 49–58. [[CrossRef](#)]
57. Wang, Y.; Han, F.; Mu, J. Solidification/stabilization mechanism of Pb(II), Cd(II), Mn(II) and Cr(III) in fly ash based geopolymers. *Constr. Build. Mater.* **2018**, *160*, 818–827. [[CrossRef](#)]
58. Chen, Z.; Ye, H. Sequestration and release of nitrite and nitrate in alkali-activated slag: A route toward smart corrosion control. *Cem. Concr. Res.* **2021**, *143*, 106398. [[CrossRef](#)]
59. Lee, W.K.W.; van Deventer, J.S.J. Use of infrared spectroscopy to study geopolymerization of heterogeneous amorphous aluminosilicates. *Langmuir* **2003**, *19*, 8726–8734. [[CrossRef](#)]
60. Hajimohammadi, A.; Provis, J.L.; van Deventer, J.S.J. One-Part Geopolymer Mixes from Geothermal Silica and Sodium Aluminate. *Ind. Eng. Chem. Res.* **2008**, *47*, 9396–9405. [[CrossRef](#)]
61. Kränzlein, E.; Harmel, J.; Pöllmann, H.; Krömer, W. Influence of the Si/Al ratio in geopolymers on the stability against acidic attack and the immobilization of Pb<sup>2+</sup> and Zn<sup>2+</sup>. *Constr. Build. Mater.* **2019**, *227*, 116634. [[CrossRef](#)]
62. Zhang, Z.; Wang, H.; Provis, J.L.; Bullen, F.; Reid, A.; Zhu, Y. Quantitative kinetic and structural analysis of geopolymers. Part 1. The activation of metakaolin with sodium hydroxide. *Thermochim. Acta* **2012**, *539*, 23–33. [[CrossRef](#)]
63. Zhang, Z.; Provis, J.L.; Wang, H.; Bullen, F.; Reid, A. Quantitative kinetic and structural analysis of geopolymers. Part 2. Thermodynamics of sodium silicate activation of metakaolin. *Thermochim. Acta* **2013**, *565*, 163–171. [[CrossRef](#)]
64. Manam, J.; Das, S. Influence of Cu and Mn impurities on thermally stimulated luminescence studies of MgSO<sub>4</sub> compound. *Solid State Sci.* **2010**, *12*, 1435–1444. [[CrossRef](#)]
65. Wang, L.-Y.; Ding, F.; Zhang, Y.-H.; Zhao, L.-J.; Hu, Y.-A. Anomalous hygroscopic growth of fine particles of MgSO<sub>4</sub> aerosols investigated by FTIR/ATR spectroscopy. *Spectrochim. Acta Part A Mol. Biomol. Spectrosc.* **2008**, *71*, 682–687. [[CrossRef](#)]
66. Kuenzel, C.; Vandeperre, L.; Donatello, S.; Boccaccini, A.R.; Cheeseman, C. Ambient Temperature Drying Shrinkage and Cracking in Metakaolin-Based Geopolymers. *J. Am. Ceram. Soc.* **2012**, *95*, 3270–3277. [[CrossRef](#)]
67. Bai, C.; Deng, Y.; Zhou, Q.; Deng, G.; Yang, T.; Yang, Y. Effect of different curing methods on the preparation of carbonized high-titanium slag based geopolymers. *Constr. Build. Mater.* **2022**, *342*, 128023. [[CrossRef](#)]
68. Wu, Z.; Khayat, K.H.; Shi, C.; Tutikian, B.F.; Chen, Q. Mechanisms underlying the strength enhancement of UHPC modified with nano-SiO<sub>2</sub> and nano-CaCO<sub>3</sub>. *Cem. Concr. Compos.* **2021**, *119*, 103992. [[CrossRef](#)]
69. Irassar, E.F.; Scian, A.N.; Tironi, A. Blended Cements with Limestone Filler and Kaolinitic Calcined Clay: Filler and Pozzolanic Effects. *J. Mater. Civ. Eng.* **2017**, *29*, 1–8. [[CrossRef](#)]
70. Lv, W.; Sun, Z.; Su, Z. Study of seawater mixed one-part alkali activated GGBFS-fly ash. *Cem. Concr. Compos.* **2020**, *106*. [[CrossRef](#)]
71. Kang, C.; Kim, T. Pore and strength characteristics of alkali-activated slag paste with seawater. *Mag. Concr. Res.* **2020**, *72*, 499–508. [[CrossRef](#)]
72. Tong, L.; Zhao, J.; Cheng, Z. Chloride ion binding effect and corrosion resistance of geopolymer materials prepared with seawater and coral sand. *Constr. Build. Mater.* **2021**, *309*, 125126. [[CrossRef](#)]
73. Qu, F.; Li, W.; Dong, W.; Tam, V.W.; Yu, T. Durability deterioration of concrete under marine environment from material to structure: A critical review. *J. Build. Eng.* **2020**, *35*, 102074. [[CrossRef](#)]